

RE-ACCELERATION MODEL FOR THE ‘SAUSAGE’ RADIO RELIC

HYESUNG KANG

Department of Earth Sciences, Pusan National University, Pusan 609-735, Korea; hskang@pusan.ac.kr

Received June 30, 2016; accepted August **, 2016

Abstract: The Sausage radio relic is the arc-like radio structure in the cluster CIZA J2242.8+5301, whose observed properties can be best understood by synchrotron emission from relativistic electrons accelerated at a merger-driven shock. However, there remain a few puzzles that cannot be explained by the shock acceleration model with only in-situ injection. In particular, the Mach number inferred from the observed radio spectral index, $M_{\text{radio}} \approx 4.6$, while the Mach number estimated from X-ray observations, $M_{\text{X-ray}} \approx 2.7$. In an attempt to resolve such a discrepancy, here we consider the re-acceleration model in which a shock of $M_s \approx 3$ sweeps through the intracluster gas with a pre-existing population of relativistic electrons. We find that observed brightness profiles at multi frequencies provide strong constraints on the spectral shape of pre-existing electrons. The models with a power-law momentum spectrum with the slope, $s \approx 4.1$, and the cutoff Lorentz factor, $\gamma_{e,c} \approx 3 - 5 \times 10^4$ can reproduce reasonably well the observed spatial profiles of radio fluxes and integrated radio spectrum of the Sausage relic. The possible origins of such relativistic electrons in the intracluster medium remain to be investigated further.

Key words: acceleration of particles — cosmic rays — galaxies: clusters: general — shock waves

1. INTRODUCTION

Giant radio relics such as the Sausage and the Toothbrush relics exhibit elongated morphologies, spectral steepening across the relic width, integrated radio spectra of a power-law form with spectral curvature above ~ 2 GHz, and high polarization level (van Weeren et al. 2010, 2012; Feretti et al. 2012; Stroe et al. 2016). They are thought to be synchrotron radiation emitted by GeV electrons, which are (re)-accelerated at structure formation shocks in the intracluster medium (ICM) (e.g., Ensslin et al. 1998; Brüggen et al. 2012; Brunetti & Jones 2014). It is now well established that nonthermal particles can be (re)-accelerated at such shocks via diffusive shock acceleration (DSA) process (e.g., Ryu et al. 2003; Vazza et al. 2009; Skillman et al. 2011; Kang & Ryu 2011).

In the simple DSA model of a steady planar shock, the synchrotron radiation spectrum at the shock becomes a power-law of $j_\nu(r_s) \propto \nu^{-\alpha_{\text{sh}}}$ with the *shock index*, $\alpha_{\text{sh}} = (M_s^2 + 3)/2(M_s^2 - 1)$, while the volume-integrated radio spectrum becomes $J_\nu \propto \nu^{-\alpha_{\text{int}}}$ with the integrated index, $\alpha_{\text{int}} = \alpha_{\text{sh}} + 0.5$, above the break frequency ν_{br} (e.g. Drury 1983; Ensslin et al. 1998; Kang 2011). Here M_s is the shock sonic Mach number. If the shock acceleration duration is less than ~ 100 Myr, however, the break frequency, $\nu_{\text{br}} \sim 1$ GHz, falls in the typical observation frequencies and the integrated spectrum steepens gradually over the frequency range of $(0.1 - 10)\nu_{\text{br}}$ (Kang 2015b). Moreover, additional spectral curvatures can be introduced in the case of a spherically expanding shock (Kang 2015a). On the other hand, in the re-acceleration model in which the upstream gas contains a pre-existing electron popula-

tion, for example, $f_{\text{up}} \propto \gamma_e^{-s} \exp[-(\gamma_e/\gamma_{e,c})^2]$ (where γ_e is the Lorentz factor), the re-accelerated electron spectrum and the ensuing radio spectrum should depend on the slope s and the cutoff energy $\gamma_{e,c}$ as well as M_s .

Recently, Kang (2016) (Paper I) has explored the observed properties of the Toothbrush relic, and also reviewed some puzzles in the DSA origin of radio *gishcht* relics: (1) discrepancy between M_{radio} inferred from the radio index α_{sh} and $M_{\text{X-ray}}$ estimated from the X-ray temperature discontinuities in some relics, (2) low DSA efficiency expected for weak shocks with $M_s \lesssim 3$ that form in the hot ICM, (3) low frequency of merging clusters with detected radio relics, compared to the expected occurrence of ICM shocks, and (4) shocks detected in X-ray observations without associated radio emission. In Paper I, it was suggested that most of these puzzles can be explained by the re-acceleration model in which a radio relic lights up only when a shock propagates in the ICM thermal plasma that contains a pre-existing population of electrons (see also Kang et al. 2012; Pinzke et al. 2013; Shimwell et al. 2015; Kang & Ryu 2016).

The so-called Sausage relic is a giant radio relic in the outskirts of the merging cluster CIZA J2242.8+5301, first detected by van Weeren et al. (2010). They interpreted the observed radio spectrum from 150 MHz to 2.3 GHz as a power-law-like synchrotron radiation emitted by shock-accelerated relativistic electrons. So they inferred the shock Mach number, $M_{\text{radio}} \approx 4.6$, from the spectral index at the hypothesized shock location, $\alpha_{\text{sh}} \approx 0.6$, and the magnetic field strength, $B_2 \approx 5$ or $1.2 \mu\text{G}$ from the relic width of 55 kpc. Although this shock interpretation was strongly supported by observed downstream spectral aging and high polarization levels, the requirement for a relatively high Mach num-

ber of $M_s = 4.6$ in the ICM called for some concerns. Based on structure formation simulations, the shocks in the ICM are expected to have low Mach numbers, typically $M_s < 3$ (e.g., Ryu et al. 2003).

Stroe et al. (2014b) reported that the integrated spectrum of the Sausage relic steepens toward 16 GHz with the integrated index increasing from $\alpha_{\text{int}} \approx 1.06$ to $\alpha_{\text{int}} \approx 1.33$ above 2.3 GHz. They noted that such a curved integrated spectrum cannot be consistent with the simple DSA model for a steady plane shock with $M_s \approx 4.6$ suggested by van Weeren et al. (2010). Later, Stroe et al. (2014a) suggested, using a spatially resolved spectral fitting, that the injection index could be larger, i.e., $\alpha_{\text{sh}} \approx 0.77$, implying $M_s \approx 2.9$. In fact, this lower value of M_s is more consistent with temperature discontinuities detected in X-ray observations by Ogorean et al. (2014) and Akamatsu et al. (2015).

In order to understand the spectral curvature in the integrated spectrum reported by Stroe et al. (2014b), Kang & Ryu (2015) considered the various shock models including both the *in-situ injection* model without pre-existing electrons and the *re-acceleration* model with pre-existing electrons of a power-law spectrum with exponential cutoff. It was shown that shock models with $M_s \approx 3$, either the *in-situ injection* or the *re-acceleration* models can reproduce reasonably well the radio brightness profile at 600 MHz and the curved integrated spectrum of the Sausage relic except the abrupt increase of the spectral index above 2 GHz. The authors concluded that such a steep increase of the spectral index cannot be explained by the simple radiative cooling of postshock electrons. On the other hand, it was pointed out that the Sunyaev-Zeldovich effect may induce such spectral steepening by reducing the radio flux at high frequencies by a factor of two or so (Basu et al. 2015).

Recently, Stroe et al. (2016) presented the integrated spectrum spanning from 150 MHz up to 30 GHz of the Sausage relic, which exhibits a spectral steepening from $\alpha_{\text{int}} \approx 0.9$ at low frequencies to $\alpha_{\text{int}} \approx 1.71$ above 2.5 GHz. Kang & Ryu (2016) attempted to reproduce this observed spectrum by the re-acceleration model in which a spherical shock sweeps through and then exits out of a finite-size region with pre-existing relativistic electrons. Since the re-acceleration stops after the shock crosses the region with pre-existing electrons, the ensuing integrated radio spectrum steepens much more than predicted for aging postshock electrons alone, resulting in a better match to the observed spectrum. We suggested that a shock of $M_s \approx 2.7 - 3.0$ and $u_s \approx 2.5 - 2.8 \times 10^3 \text{ km s}^{-1}$ that has swept up the cloud of $\sim 130 \text{ kpc}$ with pre-existing electrons about 10 Myr ago, could reproduce the observed radio flux profile at 600 MHz (van Weeren et al. 2010) and the observed integrated spectrum (Stroe et al. 2016). The required spectral shape of pre-existing electrons is a power-law spectrum with the slope, $s = 4.2$ and the exponential cutoff at $\gamma_{e,c} \approx 10^4$.

On the other hand, Donnert et al (2016) has proposed an alternative approach to explain the spectral

steepening of the Sausage relic. In order to match the observed brightness profiles, it was assumed that behind the shock the magnetic field strength increases first, peaks around 40 kpc from the shock and then decreases exponentially at larger distances. In this model, the magnetic field strength is lower at the immediate postshock region with the highest energy electrons, compared to the model with constant postshock magnetic field. As a result, the integrated radio spectrum steepens at high frequencies, leading to the curved spectrum consistent with the observation by Stroe et al. (2016).

That paper presented beam convolved brightness profiles, $S_\nu(R)$, at several radio frequencies from 153 MHz to 30 GHz in their Figure 5 and the spectral index, α_{153}^{608} between 153 and 608 MHz in Figure 6. We notice that S_ν at 153 – 323 MHz extends well beyond 150 kpc away from the relic edge, and α_{153}^{608} increases from ~ 0.6 at the position of the putative shock to ~ 1.9 at 200 kpc south of the shock. Considering the shock compression ratio of $\sigma \approx 3$, these downstream length scales imply that the shock has swept through a region of at least 450 kpc in the case of a plane shock. So these observations cannot be explained by the model of Kang & Ryu (2016) which assumed a cloud with pre-existing electrons of 130 kpc in width.

As pointed out in Paper I, the ubiquitous presence of radio galaxies, AGN relics and radio phoenix implies that the ICM may contain radio-quiet *fossil* electrons ($\gamma_{e,c} \lesssim 10^2$) or radio-loud *live* electrons ($\gamma_{e,c} \lesssim 10^4$) (e.g., Slee et al. 2001). In the re-acceleration model, fossil electrons with $\gamma_e \sim 100$ provide seed electrons that can be injected to the DSA process and enhance the acceleration efficiency at weak ICM shocks. On the other hand, radio-loud electrons of a power-law spectrum with a cutoff at $\gamma_{e,c} \sim 7 - 8 \times 10^4$ is required to explain the broad relic width of $\sim 150 - 200 \text{ kpc}$ in the case of the Toothbrush relic (Paper I).

In our re-acceleration model of the Sausage relic, considered in Kang & Ryu (2015, 2016), the shock propagates into the thermal ICM gas with pre-existing relativistic electrons whose pressure is dynamically insignificant. Note that here the preshock medium is not a bubble of hot buoyant relativistic plasma unlike the models studied previously by Ensslin & Gopal-Krishna (2001), Ensslin & Brüggen (2002), and Pfrommer & Jones (2011). Thus the presence of pre-existing electrons does not affect the dynamics of the shock, but instead it only provides the seed electrons that can be injected effectively into the DSA process. However, it is not clear how relativistic electrons can be mixed with the thermal ICM gas, if they were to originate from radio jets and lobes ejected from AGNs. On the other hand, such a mixture of thermal gas and relativistic electrons can be understood more naturally, if they were to be produced by previous episodes of shocks and turbulence generated by merger-driven activities in the ICM (e.g., Brunetti & Jones 2014).

In this study, we attempt to explain the ob-

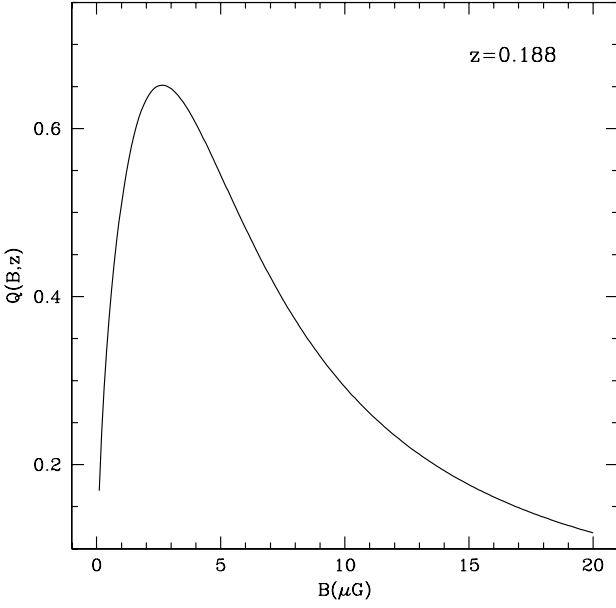


Figure 1. The factor $Q(B, z)$ for $z = 0.188$ given in Equation (4).

served properties of the Sausage relic, reported by Stroe et al. (2016) and Donnert et al (2016), with the re-acceleration model in which a low Mach number shock sweeps through the ICM gas with pre-existing relativistic electrons, as we did for the Toothbrush relic in Paper I. In the next section, we explain some basic physics of the DSA model and review the observed properties of the Sausage relic. In Section 3 the numerical simulations and the shock models are described. The comparison of our results with observations is presented in Section 4, followed by a brief summary in Section 5.

2. MODEL

2.1. Physics of DSA

The basic physical features of the DSA model for radio relics were described in detail in Paper I. Some of them are repeated here in order to make this paper sufficiently self-contained.

In the limit where the electrons that are injected *in situ* at a shock with M_s dominate over the re-accelerated electrons, the radio synchrotron spectrum at the shock position can be approximated by a power-law of $j_\nu(r_s) \propto \nu^{-\alpha_{\text{sh}}}$ with the ‘shock’ index

$$\alpha_{\text{sh}} = \frac{(M_s^2 + 3)}{2(M_s^2 - 1)}. \quad (1)$$

In the other limit where the re-accelerated electrons dominate over the injected electrons, the radio synchrotron spectrum is not a simple power-law, but depends not only on the shock Mach number but also on the spectral shape of pre-existing electrons, for in-

stance,

$$f_{\text{up}}(\gamma_e) \propto \gamma_e^{-s} \exp \left[- \left(\frac{\gamma_e}{\gamma_{e,c}} \right)^2 \right]. \quad (2)$$

Then the radio spectral index at low frequencies (~ 100 MHz) emitted by re-accelerated electrons can be approximated by $\alpha_{\text{sh}} = (s - 3)/2$, independent of M_s .

Synchrotron and inverse Compton (iC) energy losses introduce gradual spectral steepening in the volume-integrated radio spectrum behind the shock, leading to the increase of the ‘integrated’ index, α_{int} from α_{sh} to $\alpha_{\text{sh}} + 0.5$ over $\sim (0.1 - 10)\nu_{\text{br}}$. Here the break frequency depends on the magnetic field strength and the shock age as follows:

$$\nu_{\text{br}} \approx 0.63 \text{ GHz} \left(\frac{t_{\text{age}}}{100 \text{ Myr}} \right)^{-2} Q(B, z)^2. \quad (3)$$

The factor Q is defined as

$$Q(B, z) \equiv \left[\frac{(5 \mu\text{G})^2}{B^2 + B_{\text{rad}}(z)^2} \right] \left(\frac{B}{5 \mu\text{G}} \right)^{1/2}, \quad (4)$$

where $B_{\text{rad}} = 3.24 \mu\text{G}(1 + z)^2$ and B is expressed in units of μG (Kang 2011). Figure 1 shows that Q evaluated for $z = 0.188$ has the maximum value, $Q = 0.65$ at $B \approx 2.5 \mu\text{G}$.

The profiles of observed radio flux at multi frequencies can provide strong constraints on the model parameters for radio relics. For instance, the width of radio relics observed at low frequencies, whose radiation comes mainly from uncooled low energy electrons, should be similar to the advection length:

$$\Delta l_{\text{low}} \approx 100 \text{ kpc} \cdot W_l \cdot u_{2,3} \cdot \left(\frac{t_{\text{age}}}{100 \text{ Myr}} \right), \quad (5)$$

where $u_{2,3} = u_2/10^3 \text{ km s}^{-1}$ and t_{age} is the duration of the shock acceleration. The factor $W_l \sim 1.1 - 1.2$ reflects the fact that the downstream flow speed in the shock rest frame increases behind the shock in the case of a spherically expanding shock (see Figure 2 below). For planar shocks, $W_l \approx 1$.

On the other hand, the relic width at high frequencies due to cooled electrons becomes similar to the cooling length:

$$\Delta l_{\text{high}} \approx 100 \text{ kpc} \cdot W_h \cdot u_{2,3} \cdot Q \cdot \left[\frac{\nu_{\text{obs}}(1 + z)}{0.63 \text{ GHz}} \right]^{-1/2}, \quad (6)$$

where ν_{obs} is the observation frequency and the factor $W_h \sim 1.2 - 1.3$ takes account for both the downstream speed effects described above and the synchrotron radiation emitted by low energy electrons. Note that the synchrotron emission decreases smoothly behind the shock, so Equations (5) and (6) give only characteristic length scales.

Table 1. Model Parameters for the Sausage Relic Shock

Model	$M_{s,i}$	kT_1 (keV)	B_1 (μG)	s	$\gamma_{e,c}$	t_{exit} (Myr)	L_{cloud} (kpc)	t_{obs} (Myr)	$M_{s,\text{obs}}$	$kT_{2,\text{obs}}$ (keV)	$u_{s,\text{best}}$ (km s^{-1})
M3.3	3.3	3.4	1	4.1	5×10^4	124	367	144	2.7	10.7	2.6×10^3
M3.8	3.8	3.4	1	4.1	3×10^4	125	419	143	3.1	13.1	2.9×10^3

$M_{s,i}$: initial shock Mach number at the onset of the simulations

kT_1 : preshock temperature

B_1 : preshock magnetic field strength

s : power-law slope in Equation (2)

$\gamma_{e,c}$: exponential cutoff in Equation (2)

t_{exit} : time when the shock exists the cloud with pre-existing electrons

L_{cloud} : size of the cloud with pre-existing electrons

t_{obs} : shock age when the simulated results match the observations

$M_{s,\text{obs}}$: shock Mach number at t_{obs}

$kT_{2,\text{obs}}$: postshock temperature at t_{obs}

$u_{s,\text{obs}}$: shock speed at t_{obs}

2.2. Injection-dominated versus Re-acceleration dominated Model

The intracluster space may contain fossil relativistic electrons accelerated by the structure formation shocks, since the ICM is expected to go through such shocks twice or so on average (Ryu et al. 2003). In addition, there could be numerous radio galaxies and radio ghosts in the ICM (Slee et al. 2001). As a result, some cluster shocks could encounter a cloud with pre-existing relativistic electrons. Thus one can construct two limiting scenarios to explain the observations of the Sausage relic: the relic is produced (1) by the shock with $M_s \approx 4.6$ without pre-existing electrons (in-situ injection model), or (2) by the shock with $M_s \approx 3$ with pre-existing electrons with the power-law index, $s \approx 4.2$ (re-acceleration model).

In the case where in-situ injection dominates over re-acceleration, the shock Mach number should be $M_s \approx 4.6$ to explain the spectral index, $\alpha_{\text{sh}} \approx 0.6$ at the edge of the Sausage relic. Then the postshock temperature would be $kT_2 = 20.2$ keV (for $kT_1 = 2.7$ keV), which is well above the observed postshock temperature, $8.5^{+0.8}_{-0.6}$ keV (Akamatsu et al. 2015). So we disfavor this in-situ injection model mainly because of the discrepancy in the postshock temperature. Moreover, $M_s = 4.6$ is rather high for typical shocks ($M_s \lesssim 2$) that are expected to form in the hot ICM during the course of cluster mergers (e.g. Ryu et al. 2003). However, we note that Donnert et al (2016) argue that, based on the in-situ injection model, the observed brightness profiles can be modeled only with the postshock flow speed, $u_2 \gtrsim 1200$ km s^{-1} . For the $M_4 = 4.6$ model the shock speed becomes $u_s = 4.1 \times 10^3$ km s^{-1} , and the downstream flow speed is estimated to be $u_2 = 1.2 \times 10^3$ km s^{-1} .

In the re-acceleration model, on the other hand, one can adjust the pre-existing electron spectrum in order to reproduce the observed radio brightness profiles and the integrated spectrum. For example, the power-law

index should be $s \approx 4.2$ to match the observed value, $\alpha_{\text{sh}} \approx 0.6$ at the edge of the Sausage Relic. One of the advantages of this model is the fact that, independent of α_{sh} , we can adopt a low Mach number ($M_s \lesssim 3$), which is more compatible with X-ray observations. The cutoff energy, $\gamma_{e,c}$, also controls how fast the electron spectrum steepens behind the shock, so it can be adjusted to reproduce the observed spectral aging in the downstream region.

2.3. Observed Properties of the Sausage Relic

The cluster CIZA J2242.8+5301 that hosts the Sausage relic is estimated to be located at the redshift, $z = 0.188$ (Dawson et al. 2015). According to the Suzaku X-ray observations, the ICM temperature drops from $kT_2 = 8.5^{+0.8}_{-0.6}$ keV to $kT_1 = 2.7^{+0.7}_{-0.4}$ keV across the relic with the inferred shock Mach number, $M_s = 2.7^{+0.7}_{-0.4}$ (Akamatsu et al. 2015). If we take the mean observed values, the sound speed of the preshock gas with 2.7 keV is $u_1 = 8.4 \times 10^2$ km s^{-1} , so the shock speed is $u_s = 2.3 \times 10^3$ km s^{-1} for a $M_s = 2.7$ shock. With the compression ratio of $\sigma = u_1/u_2 = 2.83$, the downstream flow speed becomes $u_2 = 8.0 \times 10^2$ km s^{-1} , which is probably too slow to explain the observed relic widths (Donnert et al 2016).

The radio observations of the Sausage relic from 150 MHz to 30 GHz using various radio telescopes were reported by Stroe et al. (2016), where the flux data for the integrated spectrum was given in their Table 3. The brightness profiles of the relic at several radio frequencies based on the observations in Stroe et al. (2016) have been published recently in Donnert et al (2016). The FWHMs of the observed relic at 153 MHz and 608 MHz, measured from Figure 5 in Donnert et al (2016), are 100 kpc and 55 kpc, respectively. These radio data can be used to infer the shock parameters such M_s , u_s and B_2 according to Equations (1)-(6). According to Equation (6) with $W_h = 1.2$, $u_{2,3} = 0.8$, and $Q = 0.65$ ($B_2 = 2.5$ μG), for example, the relic width at 608 MHz is estimated to be $\Delta l_{\text{high}} \approx 58$ kpc,

which seems to be consistent with the observed profile. On the other hand, the observed brightness profile at 153 MHz extends up to 200 kpc, while the predicted cooling length is only $\Delta l_{\text{high}} \approx 116$ kpc. Thus the shock model parameters can be determined more accurately through the detail comparisons between the predicted and observed brightness profiles.

According to Figure 1 of Stroe et al. (2013), there are at least four radio galaxies, sources B, C, D, and H, within 1 Mpc from the Sausage relic, which might provide relativistic electrons to the surrounding ICM. In particular, the source H located at the eastern edge of the relic might be feeding relativistic electrons to the upstream region of the relic shock. It is not clear, however, how those electrons can be mixed with the thermal background gas as we conjecture in our model.

3. NUMERICAL CALCULATIONS

The numerical setup for our DSA simulations was described in detail in Kang (2015b). So only basic features are given here.

3.1. DSA Simulations for 1D Spherical Shocks

We follow time-dependent diffusion-convection equation for the pitch-angle-averaged phase space distribution function for CR electrons, $f_e(r, p, t) = g_e(r, p, t)p^{-4}$, in the one-dimensional (1D) spherically symmetric geometry:

$$\begin{aligned} \frac{\partial g_e}{\partial t} + u \frac{\partial g_e}{\partial r} = & \frac{1}{3r^2} \frac{\partial(r^2 u)}{\partial r} \left(\frac{\partial g_e}{\partial y} - 4g_e \right) \\ & + \frac{1}{r^2} \frac{\partial}{\partial r} \left[r^2 D(r, p) \frac{\partial g_e}{\partial r} \right] + p \frac{\partial}{\partial y} \left(\frac{b}{p^2} g_e \right), \end{aligned} \quad (7)$$

where $u(r, t)$ is the flow velocity, $y = \ln(p/m_e c)$, m_e is the electron mass, and c is the speed of light (Skilling 1975). Here r is the radial distance from the center of the spherical coordinate, which assumed to coincide with the cluster center. We assume a Bohm-like spatial diffusion coefficient, $D(r, p) \propto p/B$. The cooling term $b(p) = -dp/dt = -p/t_{\text{rad}}$ accounts for electron synchrotron and iC losses. The test-particle version of CRASH (Cosmic-Ray Amr SHock) code in a co-moving 1D spherical grid is used to solve Equation (7) (Kang & Jones 2006).

3.2. Shock parameters

We assume that the shock dynamics can be approximated by a self-similar blast wave that propagate through the isothermal ICM with the density profile of $\rho \propto r^{-2}$. So the shock radius and velocity evolves roughly as $r_s \propto t^{2/3}$ and $u_s \propto t^{-1/3}$, respectively (e.g., Ryu & Vishniac 1991).

Donnert et al (2016) chose the following shock parameters to explain the observed profiles of S_ν and α_{153}^{608} : $kT_1 = 3.0$ keV, $M_s = 4.6$, and $u_s = 4.1 \times 10^3$ km s⁻¹. Then $\sigma = \rho_2/\rho_1 = 3.5$, $kT_2 = 22.4$ keV,

and $u_2 = 1.2 \times 10^3$ km s⁻¹. Although the downstream temperature is well above the observed values, $kT_2 = 9.57_{-1.12}^{+1.25}$ keV (Ogrea et al. 2014) or $kT_2 = 8.5_{-0.6}^{+0.8}$ keV (Akamatsu et al. 2015), they adopted the high value of $M_s = 4.6$, because it is consistent with $\alpha_{\text{sh}} = 0.6$ in the in-situ injection model, and because the observed flux profiles require the downstream flow speed as large as 1.2×10^3 km s⁻¹.

Here we adopt a different set of shock parameters that may be more consistent with X-ray observations. The preshock temperature is chosen as $kT_1 = 3.4$ keV ($c_{s,1} = 0.94 \times 10^3$ km s⁻¹). Then we choose two values of the initial Mach number (see Table 1):

M3.3 model: $M_{s,i} = 3.3$, $u_{2,i} = 0.99 \times 10^3$ km s⁻¹, and $\gamma_{e,c} = 5 \times 10^4$.

M3.8 model: $M_{s,i} = 3.8$, $u_{2,i} = 1.1 \times 10^3$ km s⁻¹, and $\gamma_{e,c} = 3 \times 10^4$.

Note that the downstream flow speed in these models is smaller than the minimum value required in the in-situ injection model considered by Donnert et al (2016). So we consider several models with a range of parameters for the preshock magnetic field strength and the cutoff Lorentz factor. The preshock magnetic field strength is assumed to be $B_1 = 1$ μ G in both models, resulting in the postshock strength, $B_2 \approx 2.3 - 2.5$ μ G, since the factor $Q = 0.65$ has the greatest value for $B_2 = 2.5$ μ G. The postshock magnetic field strength is assumed to scale with the gas pressure, $B_{\text{dn}}(r) \propto \sqrt{P_g(r)}$, as in Paper I.

We find that the models with $B_1 = 1$ μ G and $\gamma_{e,c} \approx 3 - 5 \times 10^4$ produce the profiles of S_ν and α_{153}^{608} that are consistent with the observed profiles given in Donnert et al (2016). If we take smaller values for $\gamma_{e,c}$ or larger values for B_1 , for example, the simulated spectral index increases behind the shock too fast, compared to the observed profile of α_{153}^{608} .

If we take the mean value the observed value, $kT_1 = 2.7_{-0.4}^{+0.7}$ keV (Akamatsu et al. 2015), then the relevant velocities such as u_s and u_2 and the downstream length scale of radio emitting region will decrease by a factor of $\sqrt{3.4/2.7}$. For such a model, a higher value of $\gamma_{e,c}$ would be required to increase the relic width to the level that matches the observations.

In order to reproduce the steep spectral curvature above 2 GHz, we assume that the cloud with pre-existing electrons has a finite size, as in Kang & Ryu (2016). Table 1 also lists the cloud size, L_{cloud} , and the time when the shock exits the cloud, t_{exit} . Considering that the observed downstream length scale is greater than 150 kpc and the shock compression ratio is $\sigma \approx 3$, $L_{\text{cloud}} \gtrsim 400$ kpc is required. Note that this is much greater than $L_{\text{cloud}} \sim 130$ kpc adopted in Kang & Ryu (2016).

We find that both the simulated brightness profiles and the integrated spectra become consistent with the observations at the shock age of $t_{\text{obs}} \approx 144$ Myr in M3.3 model and at $t_{\text{obs}} \approx 143$ Myr in M3.8 model. The degree of spectral steepening above ~ 2 GHz is controlled by the time elapse between t_{exit} and t_{obs} . At t_{obs} the spherical shock slows down to $M_{s,\text{obs}} \approx 2.7$ with

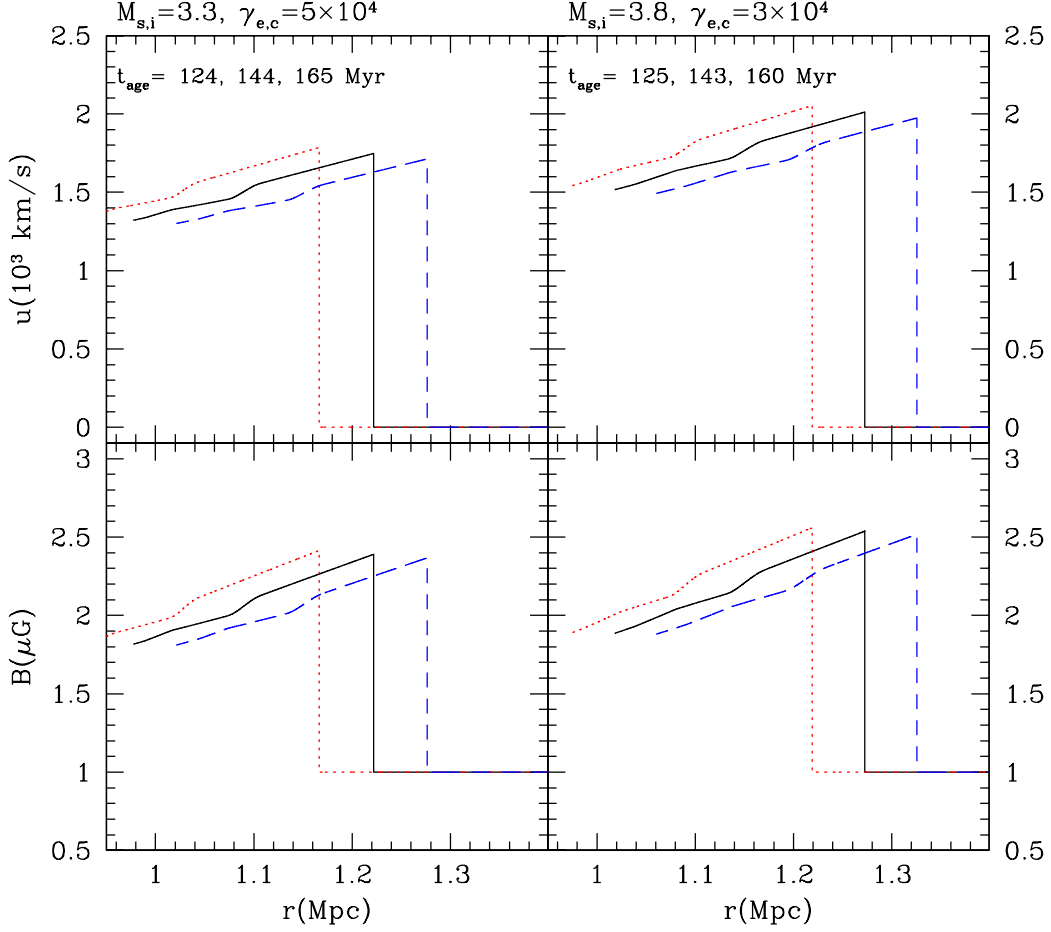


Figure 2. Flow velocity, $u(r)$, in units of 10^3 km s^{-1} (top panels), and the magnetic field strength, $B(r)$, in units of microgauss, plotted as a function of the radial distance from the cluster center, $r(\text{Mpc})$, for the M3.3 model at $t_{\text{age}} = 124$ (red dotted line), 144 (black solid), and 165 (blue dashed) Myr (left panels) and for the M3.8 model at $t_{\text{age}} = 125$ (red dotted line), 143 (black solid), and 160 (blue dashed) Myr (right panels).

$kT_{2,\text{obs}} = 10.7 \text{ keV}$ in M3.3 model, and $M_{s,\text{obs}} \approx 3.1$ with $kT_{2,\text{obs}} = 12.9 \text{ keV}$ in M3.8 model.

As mentioned in the Introduction, Kang & Ryu (2016) were able to reproduce the observed S_ν at 610 MHz (with FWHM $\sim 55 \text{ kpc}$) and the integrated spectrum of the Sausage relic with the re-acceleration models with $kT_1 = 3.35 \text{ keV}$, $M_{s,i} \approx 3.0 - 3.3$, $s = 4.2$, $\gamma_{e,c} = 10^4$, $B_1 = 2.5 \mu\text{G}$, $L_{\text{cloud}} \approx 131 \text{ kpc}$, and $t_{\text{obs}} \approx 55 \text{ Myr}$. However, such models cannot be consistent with the brightness profiles at lower frequencies (e.g., 150 MHz) that extend beyond 150 kpc behind the shock. This demonstrates that it is important to have observational data for brightness profiles at multi frequencies in addition to the integrated spectrum in order to constrain the best-fit DSA models.

4. RESULTS OF DSA SIMULATIONS

Figure 2 shows the flow speed, $u(r)$, and the magnetic field strength, $B(r)$, at three epochs: $t_{\text{age}} = 124, 144, 165 \text{ Myr}$ for M3.3 model and $t_{\text{age}} =$

125, 143, 160 Myr for M3.8 model. Here r is the radial distance from the cluster center. In both models, the shock is about to exist the cloud of pre-existing electrons at $t_{\text{exit}} = 124 - 125 \text{ Myr}$ (red dotted lines), while the profiles of α_{153}^{608} and the integrated spectra become consistent with the observations of Stroe et al. (2016) at $t_{\text{obs}} = 143 - 144 \text{ Myr}$ (black solid lines) (see Figure 6). Note that the downstream flow speed in the shock rest frame increases behind the shock, while the magnetic field strength decreases in the downstream region. As a result, the cooling length, Δl_{high} , is somewhat greater than estimated for 1D planar shocks with uniform $u(r)$ and $B(r)$ in the postshock region.

Figure 3 shows the synchrotron emissivity, $j_\nu(r)$ at 153 MHz and 608 MHz in arbitrary units, and the spectral index, α_{153}^{608} in the two models. Since the shock exits the cloud of pre-existing electrons at 124 – 125 Myr, the edge of the radio relic is located slightly behind the shock for the second (black solid lines) and third (blue dashed line) epochs. For example, the relic edge is at

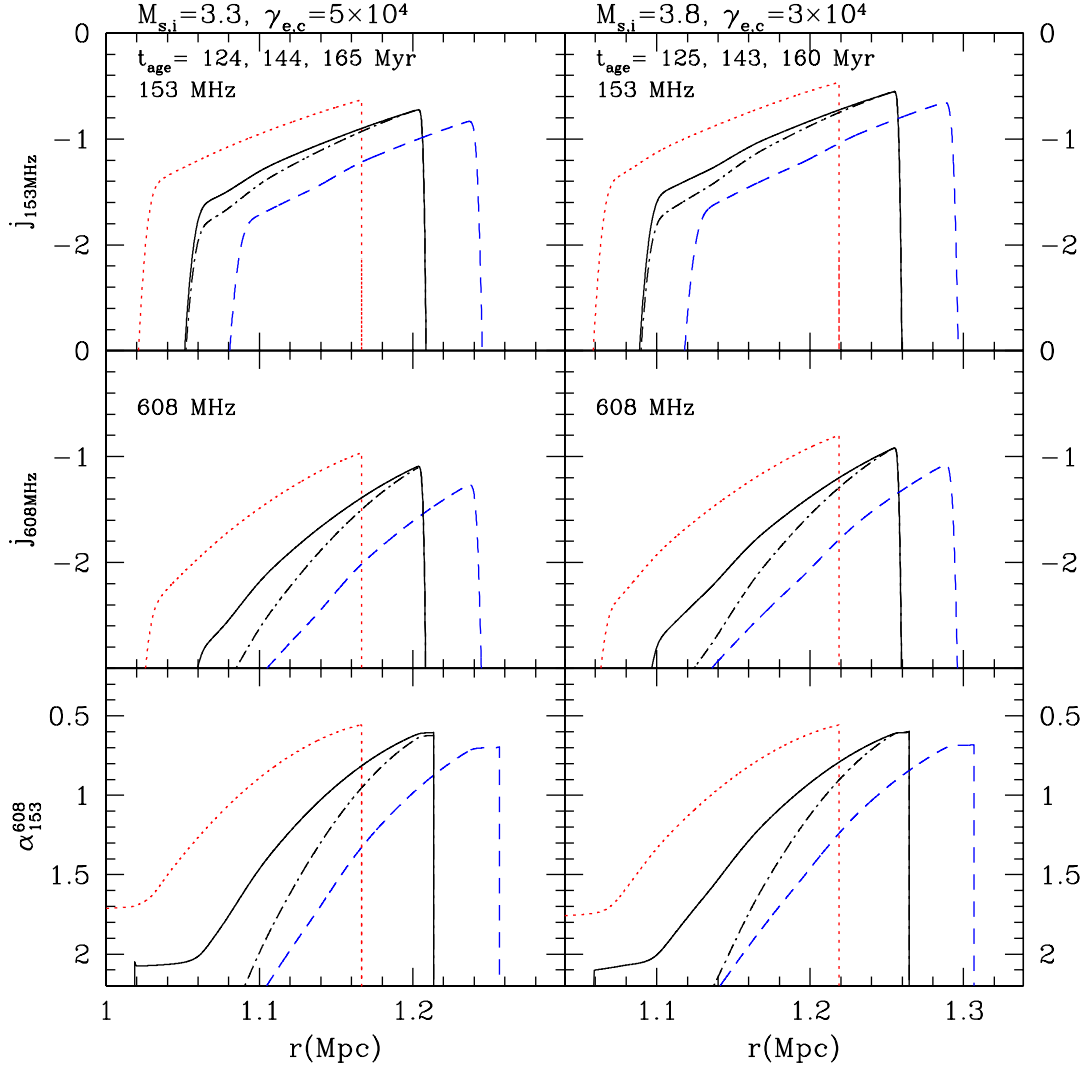


Figure 3. Time evolution of the synchrotron emissivity, $j_\nu(r)$ at 153 MHz (top panels) and 608 MHz (middle panels), and the spectral index, α_{153}^{608} between the two frequencies (bottom panels), plotted as a function of the radial distance from the cluster center, r (Mpc), for the M3.3 model (left panels) and the M3.8 model (right panels). The line types and the corresponding epochs are the same as in Fig. 2. The black dot-dashed lines show the results of the same models except higher magnetic field strength, $B_1 = 2.5 \mu\text{G}$, at the same t_{obs} .

1.162, 1.212, and 1.242 Mpc, while the shock position is at 1.162, 1.22, and 1.28 Mpc in M3.3 model.

From the profiles of $j_\nu(r)$ at 153 MHz, one can see that the advection length is 140 – 160 kpc, consistent with Equation (5). Due to faster cooling of higher energy electron $j_\nu(r)$ at 608 MHz decreases much faster with the FWHM about 50 kpc. Since the shock weakens in time, the spectral index, α_{153}^{608} , at the relic edge decreases from 0.55 to 0.7 during 125 – 165 Myr. In fact, the gradient of $\alpha_{153}^{608}(r)$ depends on the parameters, s and $\gamma_{e,c}$ as well as $M_s(t)$ and B_1 . For smaller values of $\gamma_{e,c}$ or larger values of B_1 , $\alpha_{153}^{608}(r)$ would increase behind the shock faster than that in the fiducial models shown in Figure 3. For example, the black dot-dashed lines show the results of the same models at the same t_{obs} except higher magnetic field strength, $B_1 = 2.5 \mu\text{G}$ and $B_2 \approx 5.8 - 6.3 \mu\text{G}$.

4.1. Surface Brightness and Spectral Index Profiles

The radio surface brightness, $I_\nu(R)$, is calculated from the emissivity $j_\nu(r)$ by adopting the same geometric volume of radio-emitting electrons as in Figure 1 of Kang (2015b). Here R is the distance behind the projected shock edge in the plane of the sky.

Figure 4 shows $I_\nu(R)$ at 153 MHz and 608 MHz in arbitrary units at the same time epochs as in Figure 3. Here the projection angle $\psi = 10^\circ$ is adopted. In addition, the spectral index, α_{153}^{608} is calculated from the projected $I_\nu(R)$ at 153 and 608 MHz and shown in the bottom panels. The magenta dots are observational data read from Figures 5 and 6 in Donnert et al (2016). Note that the relic edge is located 20 – 40 kpc behind the shock at the two later epochs (black solid and blue dashed lines), since the shock breaks out of the cloud

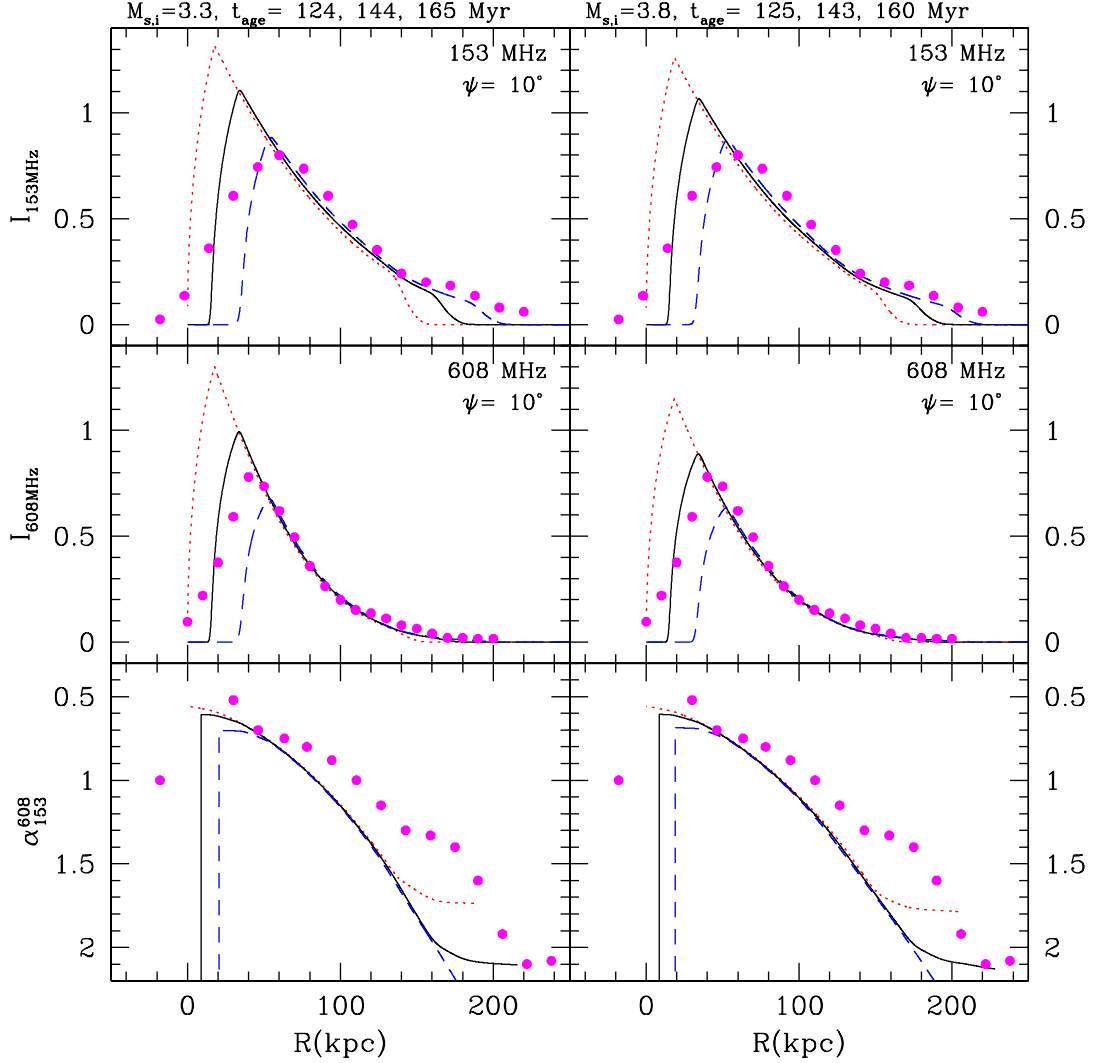


Figure 4. Time evolution of the surface brightness $I_\nu(R)$ at 153 MHz (top panels) and at 608 MHz (middle panels), and the spectral index α_{153}^{608} between the two frequencies (bottom panels) plotted as a function of the projected distance behind the shock, $R(\text{kpc})$ for the M3.3 model (left panels) and the M3.8 model (right panels). The line types and the corresponding time are the same as in Fig. 2. The projection angle, $\psi = 10^\circ$ is adopted. The magenta dots are the observational data taken from Donnert et al (2016). Note that, for the second and third epochs, the relic edge is located behind the shock (at $R = 0$).

at 124 – 125 Myr (red dotted lines).

The simulated brightness profiles can be compared with the observed data, only if the vertical scale is adjusted, since the normalization of radio brightness is arbitrary. Although the spatial profiles of I_ν at the two frequencies for $R > 40$ kpc seem to match reasonably well the observed profiles, α_{153}^{608} decreases somewhat faster than the observed trend.

In fact, the observed profiles should be compared with the brightness profiles convolved with telescope beam profile with a finite width. So we present the brightness profiles, $S_\nu(R)$, smoothed by Gaussian smoothing with 50 kpc width (a beam of 16 arcsec) at $t_{\text{obs}} = 143 - 144$ Myr in Figure 5. The simulated profiles of $S_{153\text{MHz}}(R)$ seem compatible with the observed data up to 150 kpc, beyond which they could

be contaminated by the contributions from the radio galaxies (B, C, and D) in the downstream region. For 608 MHz, $S_{608\text{MHz}}$ smoothed with 25 kpc width seems to match much better the observed profile. In the bottom panels, we also present α_{153}^{608} calculated with S_ν at the two frequencies, smoothed with 50 kpc width. The figure demonstrates that our model predictions convolved with appropriate beam widths are in reasonable agreement with the observations.

4.2. Integrated Spectrum

According to Equation (3), the break frequency at $t_{\text{obs}} = 143 - 144$ Myr is $\nu_{\text{br}} \approx 130$ MHz. So in the in-situ injection model without pre-existing electrons, the integrated radiation spectrum is expected to steepen from

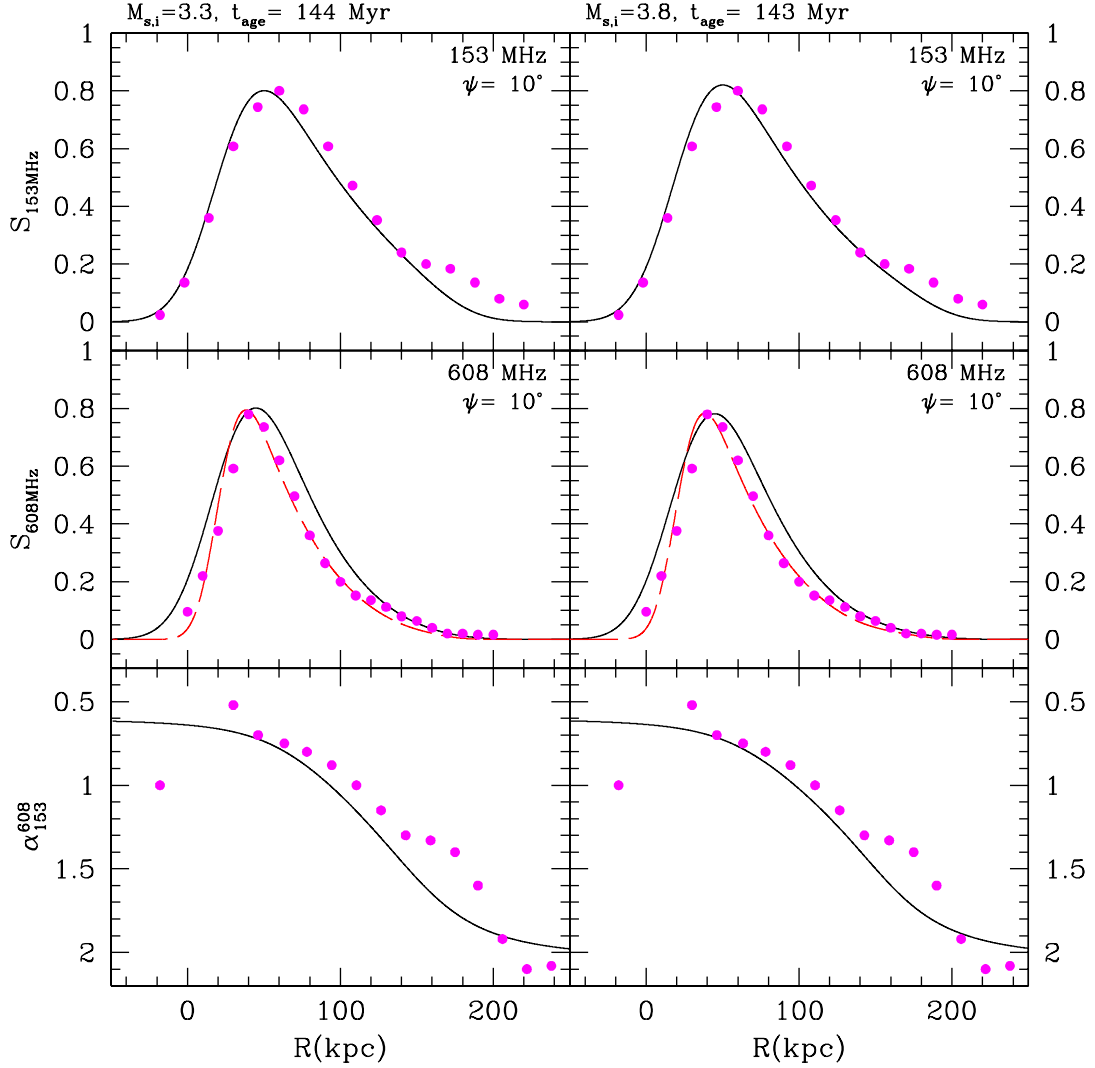


Figure 5. Beam convolved brightness profile $S_\nu(R)$ at 153 MHz (top panels) and at 608 MHz (middle panels), and the spectral index $\alpha_{0.15}^{0.61}$ between the two frequencies (bottom panels) at $t_{\text{obs}} = 144$ Myr for the M3.3 model (left panels) and at $t_{\text{obs}} = 143$ Myr for the M3.8 model (right panels). The simulated brightness profiles, $I_\nu(R)$, shown in Fig. 4 are smoothed with Gaussian smoothing with 50 kpc width in order to emulate radio observations. The brightness profile at 608 MHz smoothed with 25 kpc width is also shown by the red long dashed lines in the middle panels.

α_{sh} to $\alpha_{\text{sh}} + 0.5$ gradually over 13 MHz–1.3GHz, which is in contradiction with the observed spectrum shown in Figure 6. In the re-acceleration model, however, the integrated spectra depends also on the spectral shape of the preshock electron population. In the case of the cloud of pre-existing electrons with a finite-size, the degree of the spectral steepening also depends on the time elapse, $t_{\text{obs}} - t_{\text{exit}}$. So the spectral curvature of the observed spectrum can be reproduced by adjusting the set of model parameters, i.e., M_s , B_1 , t_{exit} , t_{obs} , s , and $\gamma_{e,c}$ in our models.

Figure 6 shows how the integrated spectrum, J_ν , steepens at higher frequencies due to lack of pre-existing seed electrons as well as radiative cooling during 131–151 Myr in the two shock models. Note again $t_{\text{exit}} = 124 - 125$ Myr. The magenta dots show the observational data taken from Table 3 of Stroe et al.

(2016), which are rescaled to fit the simulated spectrum near 1 GHz by eye. We find that $\gamma_{e,c} = 3 - 5 \times 10^4$ is needed in order to reproduce J_ν both near 1 GHz and 16–30 GHz simultaneously at t_{obs} .

5. SUMMARY

The Sausage radio relic is unique in several aspects. Its thin arc-like morphology and uniform surface brightness along the relic length over 2 Mpc could be explained by the re-acceleration model in which a spherical shock sweeps through an elongated cloud of the ICM gas with pre-existing relativistic electrons (Kang & Ryu 2015). Moreover, the re-acceleration model can resolve the discrepancy between $M_{\text{radio}} \approx 4.6$ inferred from the radio spectral index (van Weeren et al. 2010) and $M_{\text{X-ray}} \approx$

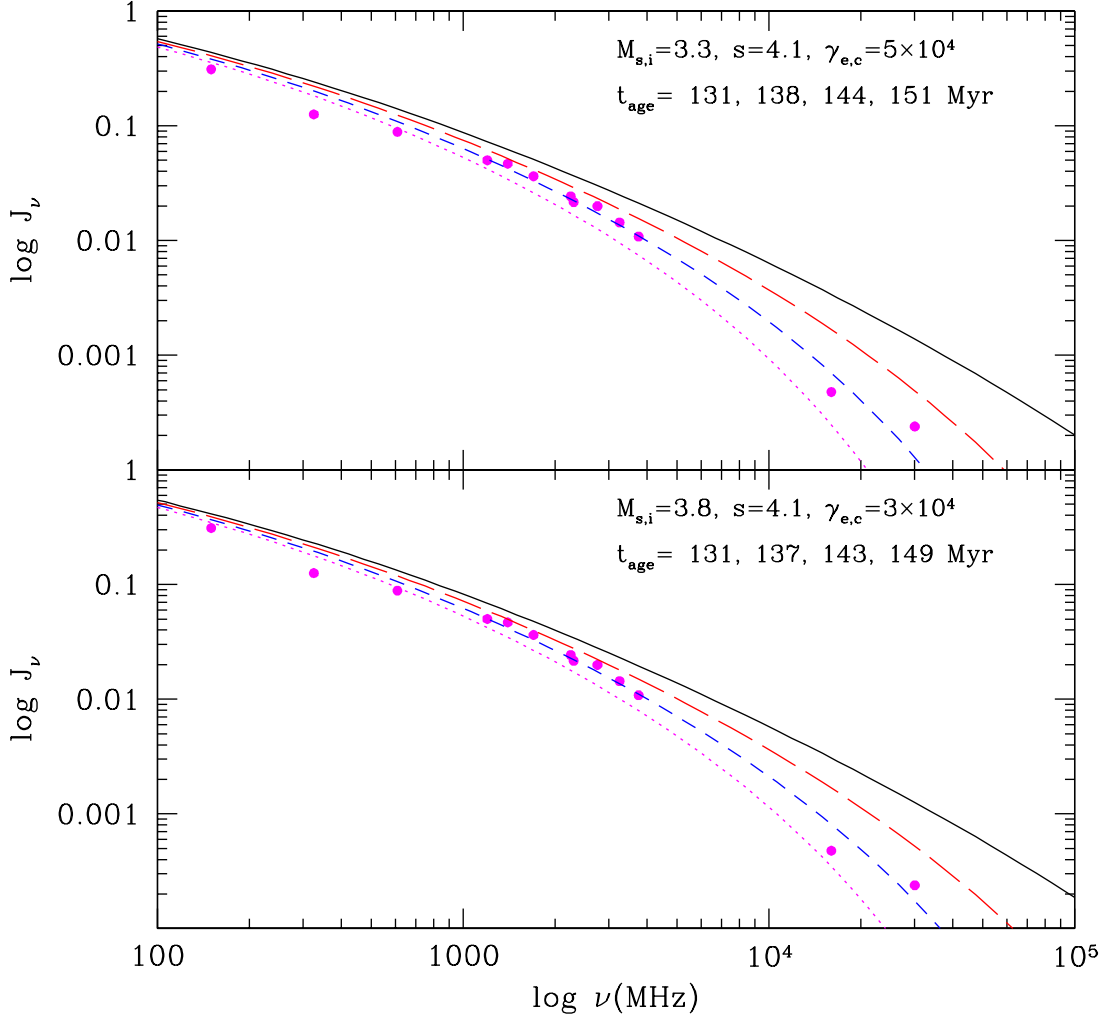


Figure 6. Time evolution of volume-integrated radio spectrum for the M3.3 model with $M_{s,i} = 3.3$ (top panel) at 131 (black solid line), 138 (red long-dashed), 144 (blue dashed), and 151 Myr (magenta dotted), and for the M3.8 model with $M_{s,i} = 3.8$ (bottom panel) at 131 (black solid line), 137 (red long-dashed), 143 (blue dashed), and 149 Myr (magenta dotted). The magenta dots are the observational data taken from Table 3 of Stroe et al. (2016).

2.7 estimated from X-ray temperature discontinuities (Akamatsu et al. 2015). Note that in this model the spectral index at the relic edge, $\alpha_{sh} \approx 0.6$, can be controlled by the power-law index of the pre-existing electron population, $s \approx 4.1 - 4.2$, independent of the shock Mach number. The steep spectral steepening above ~ 2 GHz (Stroe et al. 2016) could be understood, if we assume that the cloud of pre-existing electrons has a finite width and the shock has existed the cloud about 10 – 20 Myr ago (Kang & Ryu 2016).

In this study, we attempt to reproduce the observed profiles of the surface brightness at 153 and 608 MHz and the spectral index between the two frequencies presented in Donnert et al (2016), using the same re-acceleration model but with a set of shock parameters different from Kang & Ryu (2016). In particular, the observational facts that $S_{153\text{MHz}}$ and α_{153}^{608} extend beyond 150 kpc downstream of the shock and the degree

of spectral steepening of the integrated spectrum at high frequencies provide strong constraints to the model parameters, which are listed in Table 1. Since the re-accelerated electron spectrum depends on the pre-existing electron population, we find that the cutoff Lorentz factor should be fine tuned as $\gamma_{e,c} \approx 3 - 5 \times 10^4$ in order to match the observations.

This study illustrates that it is possible to explain most of the observed properties of the Sausage relic including the surface brightness profiles and the integrated spectrum by the shock acceleration model with pre-existing electrons. If the shock speed and Mach number are specified by X-ray temperature discontinuities, the other model parameters such as magnetic field strength and the spectral shape of pre-existing electrons can be constrained by the radio brightness profiles at multi frequencies. Moreover, the degree of spectral steepening in the integrated spectrum at high

frequencies can be modeled with a finite-sized cloud with pre-existing electrons.

We assume the shock has existed the cloud of pre-existing electrons at $t_{\text{exit}} \approx 124 - 125$ Myr after crossing the length of the cloud, $L_{\text{cloud}} = 367$ kpc in M3.3 model and $L_{\text{cloud}} = 419$ kpc in M3.8 model. Although both M3.3 and M3.8 models produce the results comparable to the observations as shown in Figures 5 and 6, M3.3 model seems more consistent with X-ray observations: $M_{\text{s,obs}} = 2.7$, $kT_{2,\text{obs}} = 10.7$ keV, and $u_{\text{s,obs}} = 2.6 \times 10^3$ km s $^{-1}$ at the time of observation, $t_{\text{obs}} \approx 144$ Myr.

However, it is not well understood how an elongated cloud of the thermal gas with such pre-existing relativistic electrons could be generated in the ICM of CIZA J2242.8+5301. It could be produced by strong accretion shocks or infall shocks ($M_s \gtrsim 5$) in the cluster outskirts (Hong et al. 2014) or by turbulence induced by merger-driven activities (Brunetti & Jones 2014). Alternatively, it could originate from nearby radio galaxies, such as radio galaxy H at the eastern edge of the relic or radio galaxies B, C, and D downstream of the relic. Again it is not clear how relativistic electrons contained in jets/lobes of radio galaxies are mixed with the background gas instead of forming a bubble of hot buoyant plasma. Note that the shock passage through such relativistic plasma is expected to result in a filamentary or toroidal structure (Ensslin & Brüggen 2002; Pfrommer & Jones 2011), which is inconsistent with the thin arc-like morphology of the Sausage relic. In conclusion, despite the success of the re-acceleration model in explaining many observed properties of the Sausage relic, the origin of pre-existing relativistic electrons needs to be investigated further.

On the other hand, the in-situ injection model for radio relics has its own puzzles: (1) $M_{\text{radio}} > M_{\text{X-ray}}$ in some relics, (2) low DSA efficiency expected for weak shocks with $M_s < 3$, (3) relatively low fraction of merging clusters with detected radio relics, compared to the theoretically expected frequency of shocks in the ICM, and (4) some observed X-ray shocks without associated radio emission. In particular, the generation of suprathermal electrons via wave-particle interactions, and the ensuing enhancement of the injection to the DSA process in high beta ICM plasma should be studied in detail by fully kinetic plasma simulations.

ACKNOWLEDGMENTS

This work was supported by a 2-Year Research Grant of Pusan National University.

REFERENCES

- Akamatsu, H., van Weeren, R. J., Ogrean, G. A. et al. 2015, Suzaku X-ray study of the double radio relic galaxy cluster CIZA J2242.8+5301, *A&AP*, 582, 87
- Basu, K., Vazza, F., Erler, J., & Sommer, M. 2015, The impact of SZ effect on cm-wavelength (1-30 GHz) observation of galaxy cluster radio relics arXiv:1511.03245
- Brüggen, M., Bykov, A., Ryu, D., & Röttgering, H. 2012, Magnetic Fields, Relativistic Particles, and Shock Waves in Cluster Outskirts, *Space Sci. Rev.*, 166, 187
- Brunetti, G., & Jones, T. W. 2014, Cosmic Rays in Galaxy Clusters and Their Nonthermal Emission, *Int. J. of Modern Physics D*, 23, 30007
- Dawson W. A., Jee M. J., Stroe A. et al. 2015, MC²: Galaxy Imaging and Redshift Analysis of the Merging Cluster CIZA J2242.8+5301, *ApJ*, 805, 143
- Donnert, J. M. F., Stroe, A., Brunetti, G., et al. 2016, Magnetic Field Evolution in Giant Radio Relics using the example of CIZA J2242.8+5301, arXiv:1603.06570
- Drury, L. O'C. 1983, An Introduction to the Theory of Diffusive Shock Acceleration of Energetic Particles in Tenuous Plasmas, *Rept. Prog. Phys.*, 46, 973 CR general review
- Ensslin, T. A., Biermann, P. L., Kleing, U., & Kohle S. 1998, Cluster radio relics as a tracer of shock waves of the large-scale structure formation, *A&Ap*, 332, 395
- Ensslin, T. A., & Brüggen, M., 2002, On the formation of cluster radio relics, *MNRAS*, 331, 1011
- Ensslin, T. A., & Gopal-Krishna, 2001, Reviving fossil radio plasma in clusters of galaxies by adiabatic compression in environmental shock waves *A&Ap*, 366, 26
- Feretti, L., Giovannini, G., Govoni, F., & Murgia, M. 2012, Clusters of galaxies: observational properties of the diffuse radio emission, *A&A Rev*, 20, 54
- Hong, E. W., Ryu, D., Kang, H., & Cen, R. 2014, Shock Waves and Cosmic Ray Acceleration in the Outskirts of Galaxy Clusters, *ApJ*, 785, 133
- Kang, H. 2011, Energy Spectrum of Nonthermal Electrons Accelerated at a Plane Shock, *JKAS*, 44, 49
- Kang, H. 2015a, Nonthermal Radiation from Relativistic Electrons Accelerated at Spherically Expanding shocks, *JKAS*, 48, 9
- Kang, H. 2015b, Radio Emission from Weak Spherical Shocks in the Outskirts of Galaxy Clusters, *JKAS*, 48, 155
- Kang, H. 2016, Re-acceleration model for the 'Toothbrush' Radio Relic, *JKAS*, 49, 83 (Paper I)
- Kang, H., & Jones, T. W. 2006, Numerical Studies of Diffusive Shock Acceleration at Spherical Shocks, *Astropart. Phys.*, 25, 246
- Kang, H., & Ryu, D. 2011, Re-acceleration of Non-thermal Particles at Weak Cosmological Shock Waves, *ApJ*, 764, 95
- Kang, H., & Ryu, D. 2015, Curved Radio Spectra of Weak Cluster Shocks, *ApJ*, 809, 186
- Kang, H., & Ryu, D. 2016, Re-acceleration Model for Radio Relics with Spectral Curvature, *ApJ*, 823, 13
- Kang, H., Ryu, D., & Jones, T. W. 2012, Diffusive Shock Acceleration Simulations of Radio Relics, *ApJ*, 756, 97
- Ogrean, G. A., Brüggen, M., van Weeren, R., et al. 2014, Multiple density discontinuities in the merging galaxy cluster CIZA J2242.8+5301 *MNRAS*, 440, 3416
- Pinzke, A., Oh, S. P., & Pfrommer, C. 2013, Giant radio relics in galaxy clusters: re-acceleration of fossil relativistic electrons?, *MNRAS*, 435, 1061
- Pfrommer, C., & Jones, T. W. 2011, Radio Galaxy NGC 1265 Unveils the Accretion Shock Onto the Perseus Galaxy Cluster, *ApJ*, 730, 22
- Ryu, D., Kang, H., Hallman, E., & Jones, T. W. 2003, Cosmological Shock Waves and Their Role in the Large-Scale Structure of the Universe, *ApJ*, 593, 599
- Ryu, D., & Vishniac, E. T. 1991, The dynamic instability of adiabatic blast waves, *ApJ*, 368, 411
- Shimwell, T. W., Markevitch, M., Brown, S., Feretti, L, et al., 2015, Another Shock for the Bullet Cluster, and the

- Source of Seed Electrons for Radio Relics, *MNRAS*, 449, 1486
- Skilling, J. 1975, Cosmic Ray Streaming. I - Effect of Alfvén Waves on Particles, *MNRAS*, 172, 557
- Skillman, S. W., Hallman, E. J., O’Shea, W., Burns, J. O., Smith, B. D., & Turk, M. J. 2011, Galaxy Cluster Radio Relics in Adaptive Mesh Refinement Cosmological Simulations: Relic Properties and Scaling Relationships, *ApJ*, 735, 96
- Slee O. B., Roy A. L., Murgia M., Andernach H., & Ehle M., 2001, Four Extreme Relic Radio Sources in Clusters of Galaxies, *AJ*, 122, 1172
- Stroe, A., van Weeren, R. J., Intema, H. T., Röttgering, H. J. A., Brüggen, M., & Hoeft, M. 2013, Discovery of spectral curvature in the shock downstream region: CIZA J2242.8+5301, *A&Ap*, 555, 110
- Stroe, A., Harwood, J. J., Hardcastle, M. J., & Röttgering, H. J. A. 2014a, Spectral age modelling of the ‘Sausage’ cluster radio relic, *MNRAS*, 455, 1213
- Stroe, A., Rumsey, C., Harwood, J. J., van Weeren, R. J., Röttgering, H. J. A., et al. 2014b, The highest frequency detection of a radio relic: 16 GHz AMI observations of the ‘Sausage’ cluster, *MNRAS*, 441, L41
- Stroe, A., Shimwell, T. W., Rumsey, et al. 2016, The widest frequency radio relic spectra: observations from 150 MHz to 30 GHz, *MNRAS*, 455, 2402
- van Weeren, R., Röttgering, H. J. A., Brüggen, M., & Hoeft, M. 2010, Particle Acceleration on Megaparsec Scales in a Merging Galaxy Cluster, *Science*, 330, 347
- van Weeren, R., Röttgering, H. J. A., Intema, H. T., Rudnick, L., Brüggen, M., Hoeft, M., & Oonk, J. B. R. 2012, The “Toothbrush-relic”: evidence for a coherent linear 2-Mpc scale shock wave in a massive merging galaxy cluster?, *A&AP*, 546, 124
- Vazza, F., Brunetti, G., & Gheller, C. 2009, Shock waves in Eulerian cosmological simulations: main properties and acceleration of cosmic rays, *MNRAS*, 395, 1333